Modelling the effects of boundary proximity on a tidal stream turbine using the actuator line method

Huw A. Edwards, Xiaosheng Chen, Christopher R. Vogel, and Richard H. J. Willden

Abstract—**It is well recognized that a tidal turbine's power generating potential can be improved by utilising flow constriction effects generated by proximity to a fluid boundary or other turbines in a co-planar fence. Previous experimental studies have identified load fluctuations associated with blades passing near flow boundaries, while numerical studies have analysed the flow characteristics and rotor performance of co-planar turbine arrays using azimuthally-averaged rotor modelling techniques. This study aims to bridge this gap by employing a discrete blade representation of the rotor, through an actuator line model embedded in a Reynolds-Averaged Navier-Stokes solver, to study the effects of varying proximity to a non-deformable upper boundary. The simulations used an immersed boundary method for the nacelle representation and a Wimshurst-type tip-loss model. These models are validated by comparison against both experimental data, and other simulation results using a nacelle resolved mesh and the Shen-type tip correction model. It is found that decreasing the tip clearance from 1.188 to 0.063 rotor diameters, increases the maximum power coefficient by $\sim$1%, but introduces a once-per-revolution loading cycle in root bending moments of $\sim$3% relative to mid-depth mean values. Azimuthal variations in the rotor plane streamwise and whirl velocities are found to impact the sampled angle of attack and relative velocity magnitude, which ultimately results in azimuthally varying blade loads. The root bending moments in the flapwise direction are found to be dominated by variations in relative velocity magnitude, whereas the loads in the edgewise direction show much greater dependence on angle of attack variation.**

Index Terms—**Boundary proximity, tidal turbine hydrodynamics, actuator line method, CFD**

I. Introduction

TIDAL stream energy shows promise, particularly in the UK, in providing a predictable contribution to national base load requirements, and in decarbonising the energy sources of remote communities [1]. However, to expand deployment and realise this potential, reductions in the levelised cost of energy are required to compete against other renewable energy sources [2]. Cost reductions may come from improved performance to increase the efficiency of energy production, reduction in maintenance costs, or reduction in capital costs through less conservative design. Greater energy extraction can be achieved by utilising constructive hydrodynamic phenomena between neighbouring turbines and with fluid domain boundaries, or by operating at the top of the water column where flow speeds are highest [3]. Further, operation and maintenance costs can be reduced by locating turbines close to the surface, for example by supporting turbines from floating platforms, allowing easier access compared to seabed mounted devices. However, operating in the vicinity of another turbine or a fluid boundary introduces additional azimuthal variations to the flow environment leading to unsteady blade loads which can increase the fatigue damage rate necessitating more robust blade design [4]. Before utilising constructive interference effects, the performance changes and unsteady loads must be quantified to inform a cost benefit analysis.

For a turbine in unconstrained flow, the maximum power coefficient (C_P) is limited to $16/27$ of the undisturbed kinetic energy flux through the rotor area [5]. This maximum, often referred to as the Betz limit, occurs when the rotor presents the optimum resistance to the incoming flow, imparting enough force to maximise power without overly choking the flow through the rotor. However, in the context of tidal stream energy, the flow is often constrained by the seabed and the free surface changing the balance of optimal rotor resistance. Thus, the limit for maximum power extraction is modified to the form first presented by Garrett and Cummins, $C_P = (16/27)(1-B)^{-2}$ [6]. The factor B, known as the blockage ratio, represents the fraction of the channel cross-section occupied by the rotor swept area, and allows rotors operating in confined conditions to theoretically exceed the Betz limit. A typical assumption is that the turbine is centred in the domain such that the blockage is isotropic, although some studies have investigated the effects of channel aspect ratio [7], [8].

Subsequent theoretical work by Nishino and Willden extended this model to demonstrate that constructive interference effects between closely spaced turbines in a co-planar fence can allow efficiency increases above the Betz limit, even in an infinitely wide channel where the overall blockage ratio is negligible [9]. This phenomenon has been observed by several studies both experimentally, and numerically using actuator disk and blade element momentum methods [4], [10]–[12]. However, there have been limited investigations of the azimuthal load variations caused by local flow passage anisotropy; see for example [4]. Further, the nature of experimental investigations limits the availability of

H. A. Edwards, X. Chen, C. R. Vogel and R. H. J. Willden are with the Department of Engineering Science, University of Oxford, Oxford OX1 3PJ (email: huw.edwards@eng.ox.ac.uk).

Digital Object Identifier:
https://doi.org/10.36688/ewtec-2023-407

detailed flow field data.

In this study, a single tidal rotor is simulated using the actuator line (AL) model embedded in a Reynolds-Averaged Navier-Stokes (RANS) solver with varying degrees of flow passage anisotropy imposed by proximity to a non-deformable upper boundary. The investigation is carried out in the context of the Supergen ORE Unsteady Tidal Turbine Benchmarking Project using a 1.6 m rotor in a computational domain equivalent to the towing tank dimensions at the QinetiQ Haslar facility in which the turbine was tested experimentally [13]. The discrete blade representation and unsteady nature of the AL method allows investigation of the spanwise load distributions and local flow parameters at different positions around the azimuth – data which are not available from steady state methods such as blade element momentum theory or actuator disk theory used in previous numerical studies.

The objective of this study is to analyse these azimuthally and spanwise varying data outputs alongside flow field data in order to enhance understanding of the physics responsible for changes in rotor performance and unsteady blade loading that occur due to boundary proximity. The first section describes the methodology employed to extract this data including details of the turbine geometry and computational domain, the actuator line method, and an iterative procedure used to find the optimal operating point without excessive computational cost. The model setup is validated against experimental data before discussing results in terms of the average rotor performance, the azimuthal variations of root bending moments, and the rotor plane flow phenomena driving these unsteady loads. The relevance of this work is discussed in relation to rotor design and analysis, and the importance of resolving discrete blades when investigating unsteady blade loads.

II. Methodology

A. Turbine geometry

The study analyses the three-bladed 1.6 m diameter (D) rotor developed for the Supergen ORE Unsteady Tidal Turbine Benchmarking Project [13]. The rotor was designed using the RANS embedded Blade Element method in a cylindrical domain of equivalent blockage to the experimental tow tank facility. The design tip-speed-ratio $\lambda = R\omega/U_\infty = 6$, where R is the rotor radius, ω is the angular velocity, and U_∞ is the inflow velocity. For further detail see Tucker Harvey et al. [14].

B. Actuator Line model

The turbine rotor is modelled using an in-house AL code which represents the blades virtually as a discrete set of collocation points that are distributed along the span of each blade. At the beginning of each time step the rotor is advanced around the azimuth by an angle $\delta\theta = \omega\delta t$ where δt is the time step and θ is the azimuth angle. The flow field is then sampled at each of the collocation points and, using previously specified hydrofoil lift and drag coefficient data, the resulting blade forces determined at that instant along the span

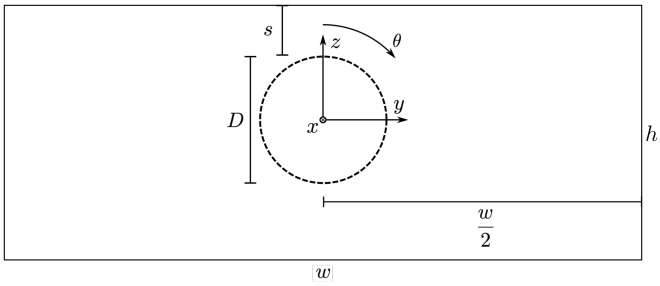

Fig. 1. The computational domain viewed from upstream of the rotor plane, i.e. the flow direction (positive x) is into the page. Key dimensions and coordinate systems are shown. w and h have lengths 7.625D and 3.375D respectively. s is varied between 1.188D and 0.063D. The turbine rotates clockwise in the positive θ direction and its circumference is represented as a dashed line.

of each blade. These forces are then imposed on the flow field and the flow momentum equations advanced in time. The solution proceeds to the next time step and so an unsteady discrete blade represented flow simulation is developed. Key parameters are the sampling radius (r_s) which defines the distance from each collocation point to flow field sampling locations, and the smearing radius (r_{sm}) which defines the region in which the computed blade forces are imposed on the flow field. The actuator line model neglects the effects of spanwise flow velocities and pressure gradients, and implicitly assumes local two-dimensional hydrofoil behaviour through the use of tabulated foil data. Additionally, spanwise loading corrections can be applied to correct for the effects of three-dimensional flow behaviour across the blade span, and results from two such corrections are presented in Section III-A.

In this study the collocation points are arranged in a cosine distribution from root to tip such that they provide greater density near the blade extremities. Eight flow field sampling points surround each collocation point, evenly distributed on a surface of constant radius from the rotor centre. The sampling points are placed on that surface at a radius $r_s = 1.1r_{sm}$ from the collocation point to avoid sampling in the disturbed region in which the force is imposed. During each iteration the flow velocity relative to the blade is determined from the simulated flow field at each collocation point by taking the linear average of the velocity at each sampling point and summing with the local blade tangential velocity. The radial component of sampled velocity is neglected. Evenly distributing the sampling points around collocation points allows the influence of the hydrofoil circulation to be eliminated in the averaging process, so that the undisturbed flow approach velocity can be determined.

The sectional blade forces at each collocation point are determined by interpolation of the input hydrodynamic data tables based on the velocity magnitude and angle of attack derived from the sampled relative velocity. The blade force is imposed on the flow using a Gaussian smearing function to apportion the force amongst the surrounding cells within a radius r_{sm} defined to be $0.99c$ where c is the local chord length. This approach is used to avoid generating a numerical singularity in the flow field.

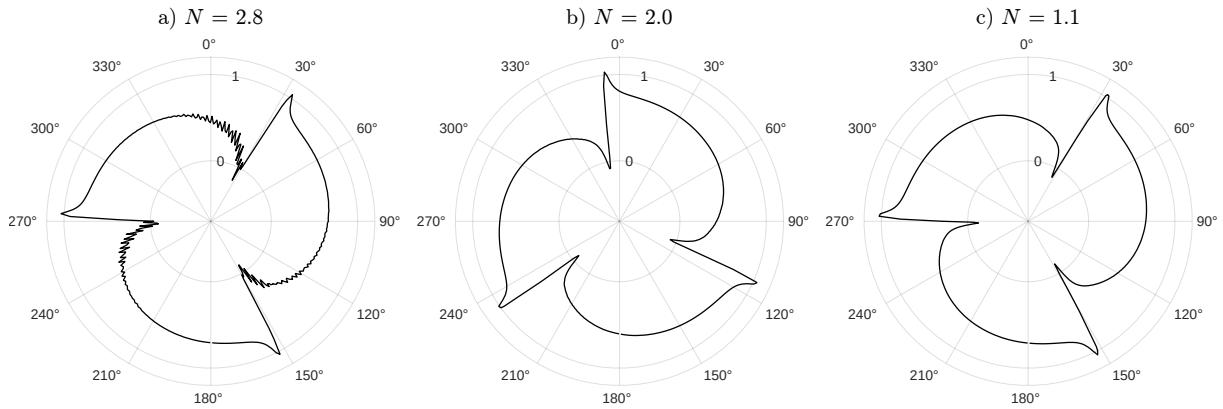

Fig. 2. Instantaneous streamwise flow velocity around the azimuth at $r/R = 0.94$. The rotor is viewed from upstream such that the blades rotate clockwise. The time step is decreasing from a) to c). The radial axis represents the streamwise flow velocity (U_x) normalised by the free stream flow velocity (U_∞).

C. Nacelle representation

The nacelle used in the experimental testing is 2.285 m in length with rounded nose cone and a cylindrical cross section of radius 0.100 m which tapers to a radius of 0.124 m just downstream of the tower. In this numerical study only the upstream 0.9 m length of the nacelle was modelled to minimise meshing complexity, and the downstream section was found to have minimal impact on rotor loads. The tower was not included as this would incur unnecessary computational cost while also introducing variable parasitic drag across the range of turbine depths to be studied. The nacelle has been modelled using both a nacelle resolving (NR) technique and an in-house version of the immersed boundary (IB) method presented by Apsley et al. developed for similar actuator line model computations [15]. The IB method has been shown to be less computationally demanding than the NR technique, while allowing very simple, quick to generate, background meshes to be used. The methods are compared in Section III-A and the IB method adopted for the boundary proximity investigation presented in this paper.

D. CFD solver

The AL code described in Section II-B was executed in OpenFOAM-v2006 using the PIMPLE algorithm to solve the RANS equations. During each solver iteration, the flow field data from the previous iteration informs the actuator line model to determine the sectional blade force which is imposed as a source term in the discretised RANS equations. The k-ω shear stress transport turbulence closure model was chosen due to its strengths in aerodynamic applications and popularity in wind and tidal turbine studies.

E. Computational setup

The computational domain replicates the cross-sectional geometry of the towing tank used to gather the experimental data for the benchmarking exercise [14] to ensure an equivalent blockage ratio of $B = 0.03$. The tank has dimensions of 12.2 m (7.625D) in the cross-stream direction (y), 5.4 m (3.375D) in the vertical direction (z), and is truncated to 48 m in the streamwise (x) direction. In the numerical model the turbine is located at a distance of 10D from the inlet and 20D from the outlet. The origin of the coordinate system remains at the rotor centre throughout the study. The rotor's position with respect to the boundary is represented by s/D where s is the tip clearance to the nearest boundary.

This study is motivated by the hypothesis that flow constriction effects established by proximity to a channel boundary may increase the performance of a tidal rotor. It is anticipated that a nearby boundary would provide additional flow constraint to the nearby region of the rotor, and work in a similar fashion to constructive interference effects seen between turbines in a co-planar fence. Therefore, free surface deformations are not considered, and the surface boundary is modelled as a non-deformable symmetry plane. Treating the boundary in this way means that the simulation also represents two counter-rotating turbines operating at an inter-turbine spacing $2s$. All surfaces of the outer domain parallel to the streamwise direction are modelled to have no viscous effects using the slip boundary condition. The inlet boundary is defined to have a fixed uniform velocity with a zero streamwise pressure gradient, while the outlet boundary has fixed uniform pressure and zero-gradient condition on velocity.

The mesh is generated using OpenFOAM's native mesh generator and is of octree type. The octree mesh contains only hexahedral elements and is structured by nature. Mesh refinement is achieved by dividing each cell dimension in half for each refinement level. The finest region is located at the rotor plane so as to accurately capture the rotor loads. Refinement is also allocated in the region downstream of the turbine so as to capture the region in which fluid shear and wake expansion effects are predicted to be significant. Cells are cuboidal with an edge length of 0.25D in the background mesh, refined down to 0.0078D in the finest region such that 128 cells span the rotor diameter at the rotor plane.

The mesh was converged spatially and temporally by evaluating the integrated rotor loads and the spanwise distribution of angle of attack. In actuator line simulations, the limiting factor constraining the maximum time step is often not the Courant number, but rather the maximum number of cells travelled by a

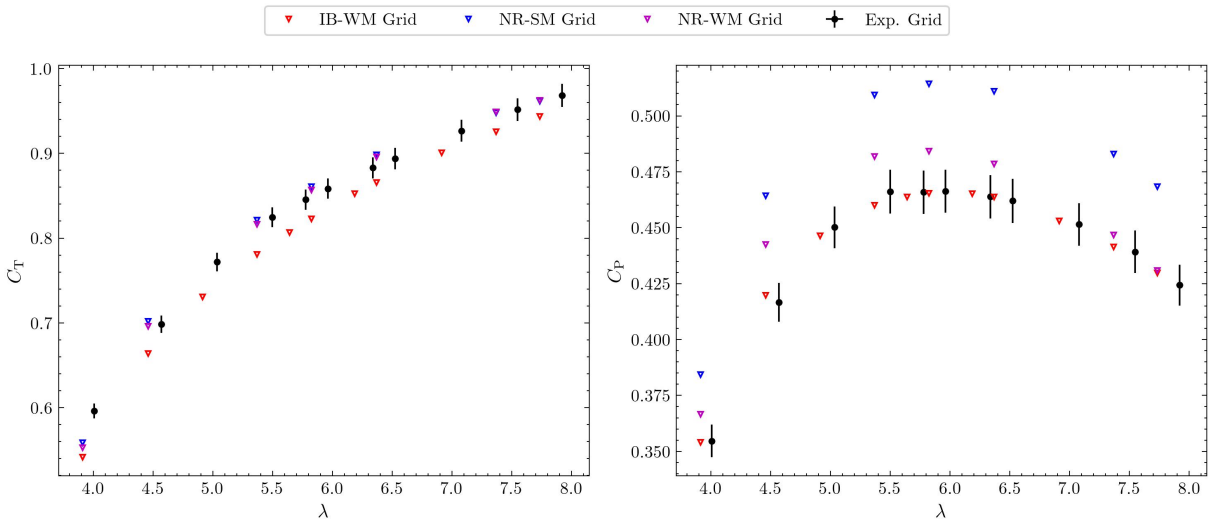

Fig. 3. Power and thrust coefficients, C_P and C_T, variation with tip-speed ratio, λ, simulated using different tip correction and nacelle representation methods against experimental data at 3% turbulence. *IB* denotes the immersed boundary method while *NR* denotes nacelle resolving. Cases labelled *WM* used the Wimshurst and Willden tip correction [16], while those labelled *SM* used the Shen et al. model [17].

collocation point during a time step (N). Fig. 2 shows the instantaneous normalised streamwise flow velocity sampled from the flow field at $r/R = 0.94$ on the rotor plane. The sampling was made close to the tip where the blade tangential velocity, and hence N, is greatest. Only the time step is varied across the cases $a) \rightarrow c)$ leaving the mesh topology unchanged. At $N = 2.8$ the streamwise velocity in the wake of the blade shows rapid fluctuations which indicate a numerical time history of where the blade has been represented in the flow field. In case $a)$ the time step is insufficiently small to deliver a continuous loading to the flow field, and the flow field in the vicinity of the blade experiences intermittent forcing of stroboscopic nature. The resultant discontinuous flow field causes errors in flow sampling such that the angle of attack on the outboard section of the blade is not correctly measured. As N is reduced the blade is more consistently represented as it moves from step to step through the mesh and so a smoother and more accurate azimuthal variation in flow speed is sampled; cases $b)$ and $c)$. In this study, it was found that $N < 2$ is sufficient to capture the angle of attack towards the tip, and to achieve a smooth continuous flow field in the wake of the simulated blade.

Each simulation is advanced in time across multiple rotations until the cycle-to-cycle time-averaged power residual remains decreasing and less than 0.01%.

III. Results

A. Model validation

Confidence in the model setup was gained by comparing simulated data against the experimental results of the Supergen ORE Unsteady Tidal Turbine Benchmarking Project. Two spanwise loading correction methods were considered: the correction factor proposed by Shen et al. [17] and the later recalibration by Wimshurst and Willden [16]. A comparison is also made between simulations representing the nacelle using the in-house IB method and a NR mesh.

The methodologies are compared in terms of the power (C_P) and the thrust (C_T) coefficients which are given by (1), where P is the rotor power, T is the rotor thrust, A is the rotor swept area, and ρ is the fluid density.

$$C_P = \frac{P}{\frac{1}{2}\rho U_\infty^3 A} \quad ; \quad C_T = \frac{T}{\frac{1}{2}\rho U_\infty^2 A} \tag{1}$$

Fig. 3 presents the simulated C_P and C_T across a sweep of tip-speed ratios compared against the experimental data. Results are shown for a rotor plane turbulence intensity of 3%, which corresponds to the *elevated turbulence* cases presented in [14] but noted as the *Grid* cases for short.

The two spanwise loading correction methods show close agreement in C_T when used with the NR mesh, both lying within 1% mean error of the experimental results. C_T decreases slightly when moving from a NR mesh to the IB method resulting in a mean under-prediction of 2.7%. This is attributed to the nacelle boundary layer representation as discussed below. Overall, the methodologies simulated show good agreement in thrust with experimental results.

Greater variation is observed in the C_P predictions. Similarly to C_T, simulations using the NR mesh generally predict a higher C_P than those using the IB method. When the Wimshurst and Willden spanwise load correction [16] was employed, the predicted C_P showed good agreement with experimental data with mean errors of 0.7% and 5% when using the NR mesh and IB method respectively. However, applying the Shen et al. load correction resulted in a 13% mean over-prediction of C_P.

The Shen et al. correction accounts for load reduction towards the blade tips by multiplying the blade forces by a function which tends to zero at the tip [17]. The correction factor is applied isotropically such that the axial force component is corrected at the same rate as the tangential force component. Wimshurst and Willden found the load reduction mechanism to be more significant in the tangential direction than the axial direction, and so recalibrated the correction factor separately in the two directions to penalise tangential

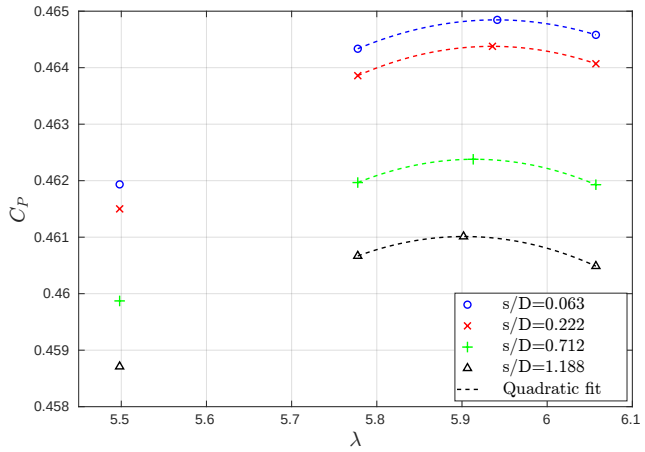

Fig. 4. Variation of C_P with λ for varying s/D.

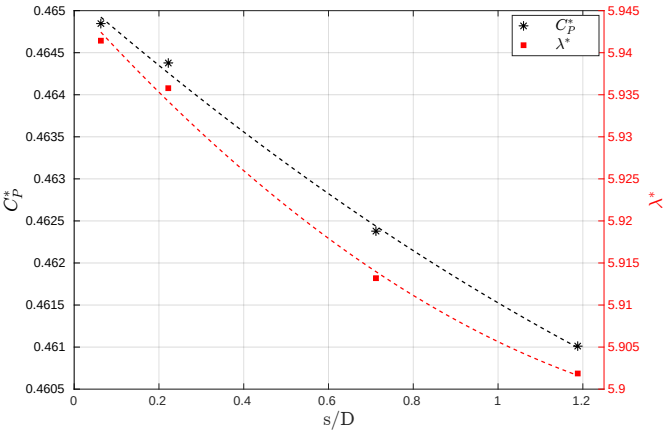

Fig. 5. Variation of C_P^* (black) and λ^* (red) with s/D.

loading at a greater rate than axial loading [16]. The difference in treatment of the tangential force is what separates the two models in their C_P predictions, with the anisotropic model peforming better.

In analysing the flow field around a nacelle in isolation (no rotor) under the same flow conditions as used in this study, it has been seen that the in-house IB method generated a significantly larger nacelle boundary layer than NR meshes of equivalent resolution. The decelerated flow near the nacelle reduces the streamwise velocity near the blade root leading to a decrease in local forces and consequently the thrust and power.

Based on the above observations, the Wimshurst and Willden loading correction was chosen. On balance, the IB method was chosen for this study to avoid the higher computational requirements of NR meshes.

B. Rotor performance

This section investigates the rotor's power and thrust performance derived from the time averaged, integrated blade loads. Simulations were carried out at 4 hub depths to range s/D between 1.188 (mid-depth) and 0.063. Following [18] an iterative process was used to determine the optimal operating point. At each rotor hub depth, three simulations are run at different tip-speed ratios, $\lambda = 5.53,\ 5.78,\ 6.06$, around the optimal value found in the experimental study. A quadratic curve is then fitted to the three time-averaged C_P-λ data points which is then used to predict the maximum power coefficient (C_P^*) and its corresponding λ. A new simulation is performed at this λ, and a quadratic curve fitted to the three highest C_P data points of the enlarged data set. This process is repeated until the new simulation C_P^* differs from the curve predicted value by less than 0.01%, at which point λ is adopted as λ^*. The iterative method was found to converge quickly. The results are summarised in Table I in terms of the maximum performance C_P^*, the thrust coefficient at which this occurs C_T^* and the rotor efficiency $\eta = C_P/C_T$ at the maximum performance point η^*.

TABLE I
ROTOR PERFORMANCE, C_P, C_T AND η, AT THE OPTIMAL OPERATING POINT (TIP-SPEED RATIO). SIMULATED C_P^*, C_T^* ARE NORMALISED BY THEIR VALUE AT $s/D = 1.188$ (MID-DEPTH).

s/D	λ^*	$C_P^*/C_{P_{mid}}^*$	$C_T^*/C_{T_{mid}}^*$	η^*
0.063	5.9414	1.0083	1.0082	0.5575
0.222	5.9358	1.0073	1.0072	0.5576
0.712	5.9132	1.0030	1.0027	0.5577
1.188	5.9019	1.0000	1.0000	0.5575

Fig. 4 shows the variation of C_P with λ across the range of tip clearances tested. The figure shows the three initial data points as well as the data point at the optimal operating condition determined by the iterative process. The dotted lines represent quadratic fits between the three highest C_P data points. In the range studied, decreasing the tip clearance by 1.125D increases C_P^* by up to 0.84% over the mid-depth case.

It is also found that optimal operation occurs at an increased λ as the rotor approaches the non-deforming surface boundary as shown in Fig. 5 which highlights that C_P^* and λ^* vary inversely with s/D. As s/D increases, the gradients of both curves decrease, so it can be inferred that the effect of boundary proximity on C_P^* and λ^* becomes ever less important as the rotor moves away from the boundary.

Decreasing s/D increases the constriction of the bypass flow adjacent to the boundary. As discussed by Vogel and Willden [12], constraining the bypass flow causes it to accelerate, reducing its static pressure. The static pressure is assumed to equalise between the bypass and the core flows at a position downstream of the rotor. Therefore, accelerating the bypass flow can result in a greater static pressure drop across the rotor, and thus a higher turbine thrust can be achieved.

Fig. 6 shows that C_T is increased at every simulated λ as s/D is decreased. The additional performance increase by a shift in optimal operating point described by [12] is also observed in the results of Fig. 6. Increasing the turbine's rotation speed increases the thrust applied to the flow. As a result, the flow rate through the rotor is reduced forcing a greater flow through the bypass. If the bypass is constrained, this results in a further increase in the static pressure drop across the turbine. Increasing the rotor plane pressure drop increases the blade forces resulting in greater blade loads. This leads to higher torque, and hence higher

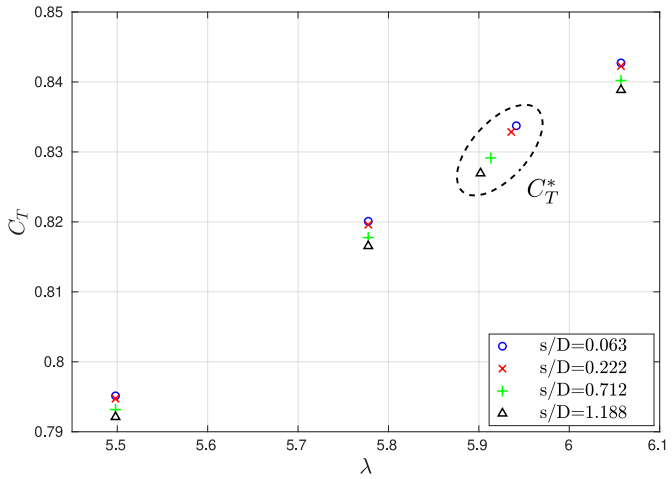

Fig. 6. Variation of C_T with λ for each s/D. C_T^* is the thrust coefficient at which the maximum power coefficient C_P^* occurs.

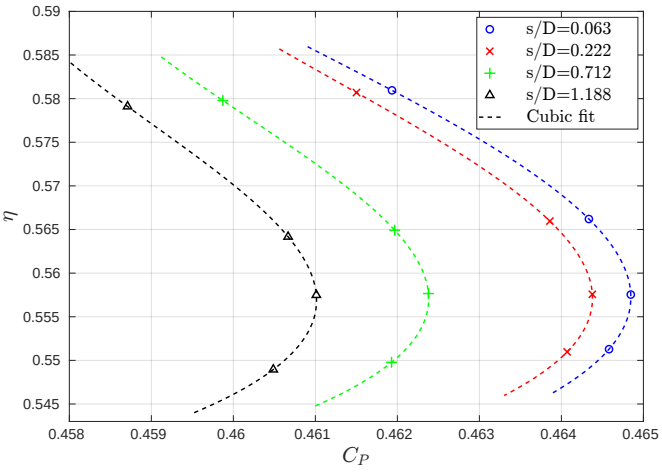

Fig. 7. Impact of boundary proximity on the variation of η with C_P. Dashed lines represent a cubic fit of the data at a given s/D.

power production for a given rotational speed [12]. As summarised in Table I, decreasing s/D consistently increases both C_P^* and the corresponding thrust coefficient C_T^*, which is achieved by λ^* moving to greater turbine rotational speeds.

Fig. 7 depicts the variation in turbine (basin) efficiency η, the ratio of the energy extracted by the turbine to the total energy removed from the flow, which can be used to measure the efficiency of resource utilisation. The total energy removed from the flow is the sum of the useful energy extracted by the turbine, and the energy lost through remixing of the core and bypass streams downstream of the turbine. Therefore, in order to maximise the basin efficiency the mixing losses must be reduced. This can be achieved by reducing the velocity differential between core and bypass flows by maximising the velocity of the core flow.

In all cases the maximum basin efficiency occurs at the lowest λ and decreases steadily as λ is increased. Due to the finite nature of the tidal resource, it may not always be practical to operate at C_P^* if this results in significant detriment to η.

Fig. 7 shows that for any given basin efficiency, the power coefficient, C_P improves with decreasing s/D. It is believed that the increasing flow constriction caused by boundary proximity drives a greater flow rate through the core of the turbine. Thus, boundary proximity effects can be utilised to extract more useful power output for a given basin efficiency. As shown in Table I, the basin efficiency at the optimal operating point (η^*) remains almost unaffected while C_P^* increases with decreasing s/D.

C. Unsteady loading

Throughout sections III-C and III-D, polar plots show the azimuthal distribution as viewed from upstream of the rotor plane such that blade rotation occurs clockwise (in the positive θ direction). Sectional blade force data can be used to derive the edgewise and flapwise root bending moments (RBMs) as a function of time, and hence space. The edgewise RBM is equivalent to torque in the θ direction, so can be interpreted as a blade's contribution to the rotor power as it moves around the azimuth. Increasing λ increased the mean flapwise RBM, but decreased the mean edgewise RBM for the range of operating points studied. At all operating points (tip-speed ratios), decreasing s/D increased both the edgewise and the flapwise loads.

Fig. 8 shows the variation of the normalised flapwise and edgewise RBMs with azimuthal position at $\lambda = 6.06$. For both cases, the RBMs are normalised against the azimuthal mean value at $s/D = 1.188$. At mid-depth the rotor loads have negligible fluctuation around the azimuth. As the rotor is brought nearer to the boundary and s/D is decreased, the interaction of each blade with the boundary becomes increasingly prominent. As seen in Fig. 8, the RBMs are greater in the upper half of the rotation where the blade is in closer proximity to the boundary. The magnitude of the peak normalised RBMs increases as s/D is decreased, with a maximum increase over the mid-depth mean of 2.64% and 1.76% in the edgewise and flapwise directions respectively. The azimuthal variations of RBMs at $s/D = 0.712$ have less defined peaks than at shallower submersion depths $s/D = 0.222, 0.063$. Rather, the RBM is generally larger than at mid-depth in the region of 270°→180° for the edgewise case, and 205°→45° for the flapwise case. The cases of $s/D = 0.222, 0.063$ are the focus of the following discussion.

The peaks in edgewise and flapwise RBM are neither in phase with each other, nor in phase with the point of closest boundary proximity at top dead centre (θ = 0°) which will be used as the reference point from which to define lead and lag angles. The flapwise RBM peaks occur in the region of θ = 330° while the edgewise RBM peaks occur around θ = 10° such that the edgewise peak lags both the point of closest surface proximity and the flapwise peak.

For the cases of $s/D = 0.222, 0.063$ at $\lambda = 5.53, 5.78, 6.06$ the phase of edgewise and flapwise RBMs are not correlated to λ or s/D with all edgewise phase angles lagging by between 5° and 9°, and flapwise phase angles leading by between 27° and 37°. However, at the optimal operating point λ^*, the degree of phase lag in edgewise RBM is higher, and increases from 18° to 25° as s/D is reduced from 0.222 to 0.063.

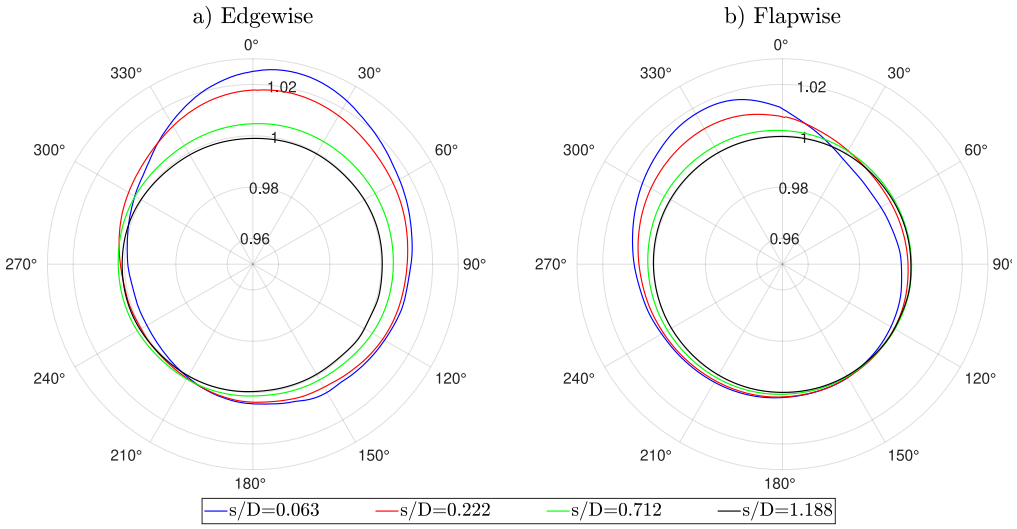

Fig. 8. The azimuthal variation of phase averaged root bending moments in the edgewise and flapwise directions for an individual blade operating at $\lambda = 6.06$. The root bending moments in each direction are plotted on the radial axis and are normalised by the azimuthally averaged value at $s/D = 1.188$ (mid-depth).

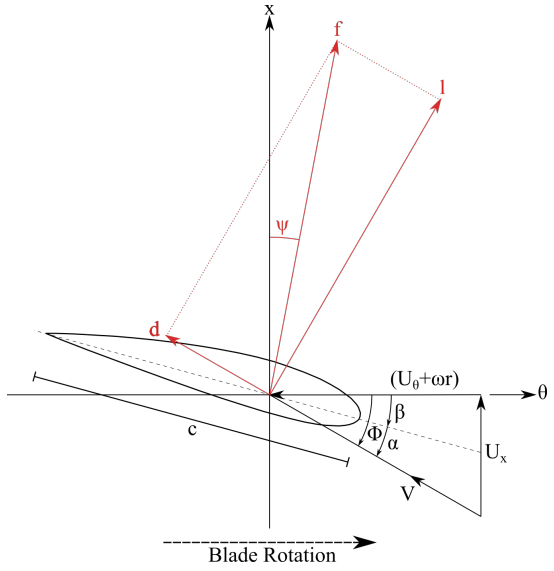

Fig. 9. An illustration of key velocity components and force vectors.

Conversely, the degree of phase lead in flapwise loads at λ^* is lower and decreases from 16° to 10° over the same change in s/D.

In addition, there are regions in which a blade experiences load alleviation relative to the mid-depth reference case. In the edgewise direction this occurs at θ between 205° and 290°, and in the flapwise direction between 15° and 135°. The load alleviations are most prominent at $s/D = 0.063$ where the edgewise and flapwise RBMs reach minima which are 0.25% and 0.59% less than the mid-depth mean respectively. Interestingly, the peaks and troughs in RBMs are not separated by a 180° phase delay for either direction.

The important conclusion for turbine designers and operators is that although boundary proximity effects can increase the yield, a once-per-revolution loading cycle is introduced which has amplitudes up to ∼3% in the edgewise direction, and ∼2.5% in the flapwise direction when normalised by azimuthal mean load. These loading fluctuations increase as the tip clearance to the surface is decreased, and will contribute to increased fatigue damage.

D. Rotor plane flow physics

This section examines the phase averaged angle of attack (α) and relative velocity magnitude ($|V|$) to investigate the previously observed load variations and the positions at which they occur. As depicted in Fig. 9, α is given by the relative inflow angle (ϕ) minus the local blade twist (β). In a fixed pitch turbine, such as the one used in this study, at each given radial location β is fixed so that ϕ, and hence α, may vary around the azimuth due to contributions from the local streamwise velocity at the rotor plane (U_x), and the local whirl velocity (U_θ).

Fig. 10 shows the azimuthal variation in α across the λ range for each s/D at 81% blade span. At this radius the blade is not subject to significant losses in blade loads from tip effects, but still results in high relative flow speeds, hence large blade forces applied with a significant lever arm, so that this location contributes significantly to the generation of root bending moments.

For all s/D at $\lambda = 5.50, 5.78$ the angle of attack always exceeds the design angle of attack ($\alpha^* = 6°$). Conversely, the angle of attack is consistently less than α^* for all s/D at $\lambda = 6.06$. It was found that λ^* for each s/D is the operating point at which the azimuthal mean angle of attack at $r/R = 0.81$ ($\bar{\alpha}_{0.81}$) is brought closest to α^*. Across the range of s/D at λ^*, the maximum deviation in $\bar{\alpha}_{0.81}$ from α^* was just 0.026° which indicates that the mean angle of attack at ∼80% span is a driving factor in achieving the maximum power coefficient. However, decreasing s/D increases $\bar{\alpha}_{0.81}$ at each specific λ which, in the cases of $\lambda = 5.50,\ 5.78$, moves $\bar{\alpha}_{0.81}$ further from α^*. Despite this, increases in C_P are still observed as s/D is decreased, so the closeness of $\bar{\alpha}_{0.81}$ to α^* cannot be considered as the only factor affecting C_P.

The increase in λ^* and C_T^* as s/D is decreased is consistent with the concept that the boundary constraint drives greater mass flux through the rotor, thus

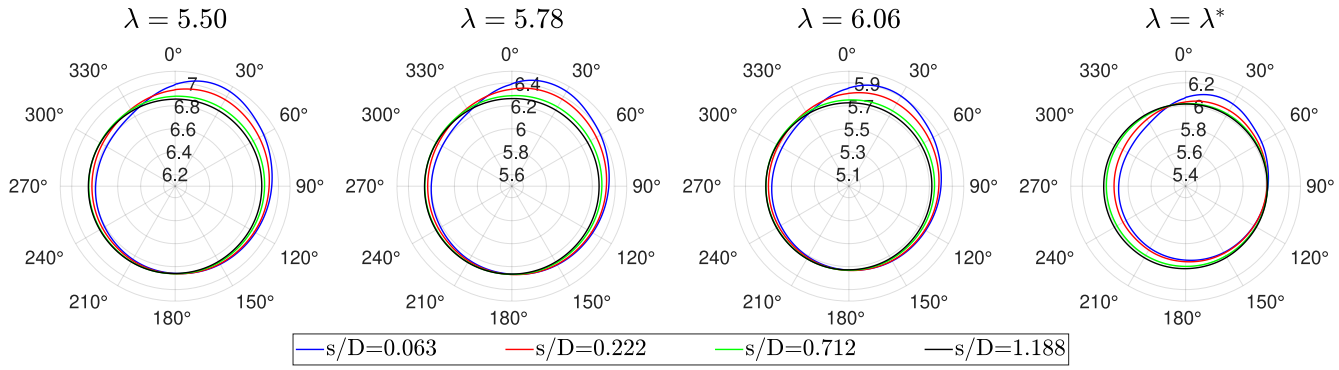

Fig. 10. The azimuthal variation of phase averaged angle of attack of the flow to the blade at $r/R = 0.81$ across the range of λ and s/D. Angle of attack is shown on the radial axis which has units of °.

enabling a higher thrust to be sustained for peak power. Increasing the rotational speed to deliver higher thrust increases the blade's tangential velocity, pushing the angle of attack back towards its optimum value.

As seen in Fig. 10, the characteristics of the azimuthal variation in α at $r/R = 0.81$ shows little change across the range of λ with standard deviations in peak phase and amplitude of 1.9° and 0.01° respectively. Therefore, the following discussion focuses on $\lambda = 6.06$.

At $r/R = 0.81$, decreasing s/D increases α such that it is greater than at $s/D = 1.188$ in the region $\theta = 330° \rightarrow 180°$. At $s/D = 0.222$, α has an amplitude of 0.14° with maxima and minima occurring at $\theta = 27°$ and $\theta = 273°$ respectively. Moving to $s/D = 0.063$ increases the amplitude to 0.24° and brings the maximum closer to top dead centre, occurring $\theta = 21°$, with the minimum at $\theta = 289°$.

Fig. 11 shows the azimuthal distibution of the relative velocity magnitude of the flow to the blade across the range of λ. At mid-depth, the mean amplitude of the velocity fluctuation at $r/R = 0.81$ is just 0.0026 m/s, which is a relative variation of 0.061%, and it is not discussed further. In general, $|V|$ is higher on the upstroke between $\theta = 180° \rightarrow 360°$. For $\lambda = 5.50, 5.78, 6.06$ the phase of maximum $|V|$ is independent of λ. As s/D is decreased the phase of peak $|V|$ shifts closer to top dead centre and occurs at 302°, 311° and 321° as s/D is progressively decreased from $0.712 \rightarrow 0.063$. However, at λ^* this peak moves to a greater θ in the cases of $s/D = 0.222$ and 0.063 so that the phase becomes 329° and 337° respectively.

In the quadrant $\theta = 0° \rightarrow 90°$ the relative velocity magnitude actually decreases such that it is less than at mid-depth. The phase of minimum $|V|$ is also independent of λ for the three initial operating points and occurs at 54°, 48° and 40° for $s/D = 0.712, 0.222$ and 0.063 respectively. For the case of λ^*, the phase of minimum $|V|$ occurs at 63° and 57° for $s/D = 0.222$ and 0.063 respectively. Therefore, the minima in $|V|$ show the same trend as the maxima for $\lambda = 5.50, 5.78, 6.06$ in that increasing surface proximity moves the extremes closer to top dead centre. The degree to which $|V|$ increases in the upper left quadrant, and $|V|$ decreases in the upper right quadrant becomes increasingly prominent as the turbine is brought closer to the surface. In the range $s/D = 0.712 \rightarrow 0.063$, the mean relative amplitude of fluctuations in $|V|$ increases from 0.27% to 2.04%.

Fig. 12 shows the time mean streamwise and whirl velocity at $r/R = 0.81$ extracted from the flow field. The flow velocities at the rotor plane are approximated by averaging the data taken from two slices upstream and downstream of the rotor plane at a distance equal to the actuator line sampling radius at $r/R = 0.81$. The whirl velocity is defined to be positive in the direction opposite to blade rotation, such that anticlockwise whirl velocity is positive in Fig. 12.

Observing the rotor plane flow field, and sampling circumferentially at radius $r/R = 0.81$ shows that the streamwise velocity through the rotor plane is generally higher on the upper half of the rotation where boundary proximity is greatest. This effect becomes more prominent as s/D is decreased with peak U_x at $s/D = 0.063$ being 1.01% greater than the peak at mid-depth. There is a bias to the downstroke side such that U_x is generally greater from $\theta = 0° \rightarrow 180°$ than from $\theta = 180° \rightarrow 360°$. On the other hand, the whirl velocity is greater between $\theta = 180° \rightarrow 360°$ than between $\theta = 0° \rightarrow 180°$, but with maxima and minima at 316° and 44° respectively. Again, the effect is most notable at $s/D = 0.063$ where the maximum and minimum U_θ are ∼129% either side of the mid-depth mean.

From the sampled flow field data, U_θ and U_x, shown in Fig. 12, it is possible to reproduce the distributions in angle of attack and relative velocity magnitude seen in figures 10 and 11 respectively, and we now concentrate on analysis of U_θ and U_x to understand azimuthal variations in root bending moments.

In the upper right quadrant the reduction in whirl velocity is more significant than the increase in streamwise velocity such that the overall relative velocity magnitude $|V|$ decreases, whilst both changes act to increase α. In the upper left quadrant both whirl and streamwise velocities increase over the mid-depth case as the turbine is brought closer to the boundary, resulting in a decrease in α and an increase in $|V|$.

The sectional lift and drag forces (l and d) are related to $|V|$, and the lift and drag coefficients (C_l and C_d) through (2), where c is the local chord length.

$$l = \frac{1}{2}\rho|V|^2 c C_l \quad ; \quad d = \frac{1}{2}\rho|V|^2 c C_d \tag{2}$$

Thus, the sectional load (f) scales with $|V|^2$, but $|V|$ has no impact on the ratio l/d. At $r/R = 0.81$, the mean sectional force in the axial direction exceeds

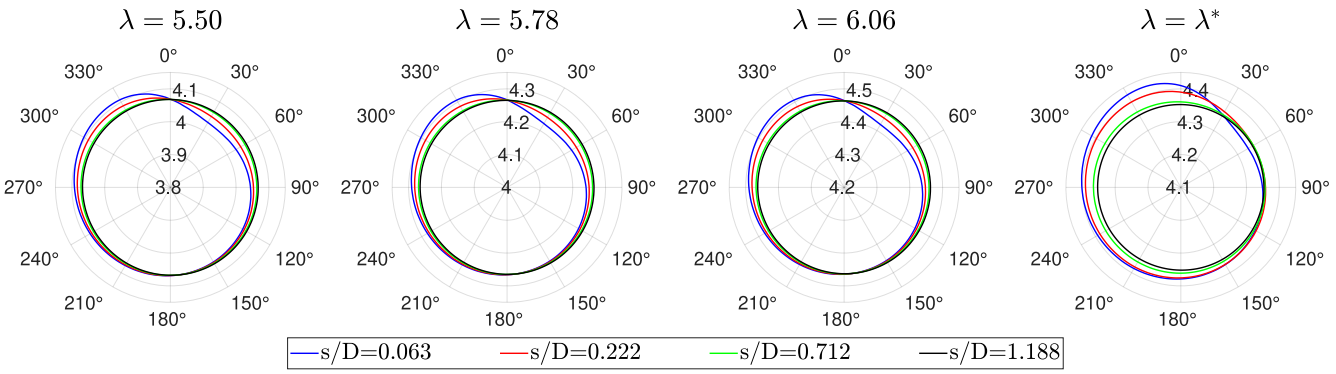

Fig. 11. The azimuthal variation of phase averaged relative velocity magnitude as sampled by the actuator line code at $r/R = 0.81$ of an individual blade across the range of λ and s/D. Relative velocity is shown on the radial axis which has units of m/s.

the tangential force by a factor of ∼9.5 such that the resultant sectional force vector is at an angle $\psi \approx 6°$ to the axial direction (see Fig. 9). The force in the flapwise direction is given by $f\cos(\psi)$ while the force in the edgewise direction is given by $f\sin(\psi)$. Hence, observing the gradients of the sine and cosine function at small angles, the edgewise force is more sensitive to changes in ψ than the flapwise force on the outboard section of the blade.

Given that the lift and drag forces are defined to be normal and parallel to the relative flow direction respectively, α influences ψ both in a rotation of the lift and drag coordinate system and in the ratio of C_l/C_d. As the deviations in angle of attack around the azimuth were small, the variations in C_l/C_d made a negligible contribution to the overall fluctuations in ψ such that the azimuthal distribution of ψ was approximately that seen in α with an amplitude of 0.253° when operating at $\lambda = 6.06$ with $s/D = 0.063$.

Taking the case of $s/D = 0.063$ at $\lambda = 6.06$ as an example, and neglecting changes in the sectional force magnitude, the fluctuations in the angle of the total sectional force vector would result in a 3.81% loading amplitude in the edgewise direction, and just a 0.05% amplitude in the flapwise direction. This equates to 161.9% of the measured RBM amplitude in the edgewise direction, but just 1.7% in the flapwise direction. Hence, the flapwise RBM is dominated by the relative velocity magnitude through its influence on the force magnitude and is insensitive to α, whereas the edgewise RBM is influenced by the relative velocity magnitude but is also highly dependant on variations in α caused by non-uniform whirl velocity. Qualitatively, this explains why the flapwise RBMs in Fig. 8 follow the velocity magnitude distribution in Fig. 11 whereas the edgewise RBMs more closely resemble the variations in α shown in Fig. 10.

IV. Discussion

It is found from the model validation that all the tested models agree reasonably well in their thrust coefficient predictions. However, the anisotropic Wimshurst-type tip-loss correction performed better in predicting the power coefficient compared to the isotropic Shen-type tip-loss correction. Also, it is found that the current version of immersed boundary method resulted in a slightly lower power coefficient compared to the nacelle resolving method. This is believed to be the result of the thicker nacelle boundary layer generated by this immersed boundary implementation.

The rigid lid model is not entirely representative of a tidal turbine in subcritical open channel flow as it assumes a negligible Froude number. Prospective tidal energy sites typically have a Froude number between 0.1 and 0.2, so a drop in the free surface height is expected as energy is extracted by the turbines [19]. However, the use of surface deformation modelling techniques such as the volume of fluid method would incur computational costs and complexity beyond the practical constraints of this study. Furthermore, the deformation of the free surface will further increase the flow constraint in the bypass, so that even greater load fluctuations and thrust and power increases are likely to occur under a deformable surface [19], [20].

Additionally, the boundary proximity strongly affected the mean angle of attack, and the mean angle of attack at 81% span was consistently less than the target angle of attack at the intended operating point. The optimal operating points were found at the rotation speeds which brought the mean angle of attack closest to the design angle of attack for each tip clearance. This highlights the importance of the flow environment and the modelling technique in the design process, and suggests that improved designs may be realised through methods using discrete blade representations.

V. Conclusions

A 1.6 m diameter experimental tidal rotor has been simulated using the RANS-AL method with an immersed boundary nacelle representation model and a Wimshurst-type tip-loss correction. The simulation technique is validated against other available models as well as the experimental results. Based on the current numerical method, a study is carried out investigating the effects of varying degrees of flow passage anisotropy imposed by proximity to a non-deformable upper boundary. The study finds that:

- Decreasing the normalised tip clearance s/D from 1.188 to 0.063 increases the maximum power coefficient by ∼1%. As s/D is decreased the optimal operating point moves to a higher tip-speed ratio as the flow constraint enables a greater thrust to be imposed with reduced impact on mass flux.

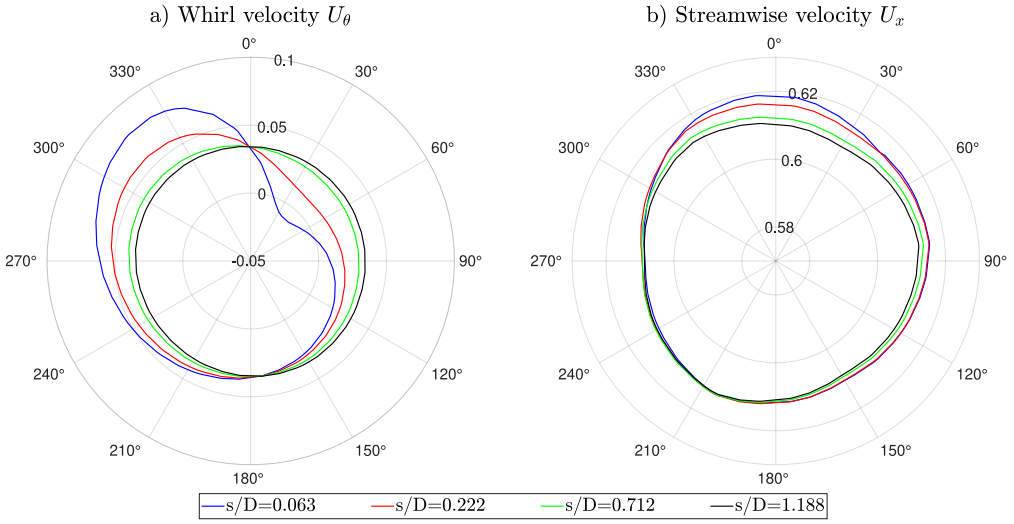

Fig. 12. The azimuthal variation of a) whirl and b) streamwise velocity components sampled at $r/R = 0.81$ from the time mean flow field at $\lambda = 6.06$ across the range of s/D. Whirl velocity is defined to be positive in the anticlockwise direction while turbine rotation is clockwise. Velocities are plotted on the radial axis which has units of m/s.

- Anisotropy in the local flow passage introduced a once-per-revolution loading cycle which increased with boundary proximity up to an amplitude of ∼3% in the edgewise direction, and ∼2.5% in the flapwise direction. At mid-depth the root bending moments were uniform around the azimuth.
- The peak in edgewise RBM lagged top dead centre, favouring the downstroke. The peak flapwise RBM occurred on the upstroke showing a phase lead to top dead centre.
- The flapwise RBM follows the azimuthal distribution of relative velocity magnitude, whereas the edgewise RBM closely resembles the azimuthal distribution of angle of attack.
- The presence of a nearby boundary increased the streamwise velocity through the adjacent half of the rotor plane. The whirl velocity was increased on the upstroke, but was decreased on the downstroke. These observations became more prominent as the tip clearance was decreased.

Acknowledgements

The authors would like to thank the Supergen ORE Hub (grant number EP/S000747/1), H.A.E.'s EPSRC scholarship (EP/S023801), C.R.V.'s UKRI Future Leaders Fellowship (MR/V02504X/1) and R.H.J.W.'s EPSRC Advanced Fellowship (EP/R007322/1) for supporting part of this research. The authors would also like to acknowledge the use of the University of Oxford's Advanced Research Computing (ARC) facility http://dx.doi.org/10.5281/zenodo.22558.

References

[1] ORE Catapult, "ReEnergise: Unleashing the power of tides," Tech. Rep., 2021.
[2] ——, "Tidal stream and wave energy cost reduction and industrial benefit," Tech. Rep., 2018.
[3] T. A. A. Adcock, S. Draper, R. H. J. Willden, and C. R. Vogel, "The Fluid Mechanics of Tidal Stream Energy Conversion," *Annual Review of Fluid Mechanics*, vol. 53, pp. 287–310, 2021.
[4] J. McNaughton, S. Ettema, F. Zilic De Arcos, C. R. Vogel, and R. H. J. Willden, "An experimental investigation of the influence of inter-turbine spacing on the loads and performance of a coplanar tidal turbine fence," *Journal of Fluids and Structures*, vol. 118, 2023.
[5] G. A. Van Kuik, "The Lanchester-Betz-Joukowsky limit," *Wind Energy*, vol. 10, no. 3, pp. 289–291, 2007.
[6] C. Garrett and P. Cummins, "The efficiency of a turbine in a tidal channel," *Journal of Fluid Mechanics*, vol. 588, pp. 243–251, 2007.
[7] T. Nishino and R. H. J. Willden, "Effects of 3-D channel blockage and turbulent wake mixing on the limit of power extraction by tidal turbines," *International Journal of Heat and Fluid Flow*, vol. 37, pp. 123–135, 2012.
[8] K. Bradley, "Performance quantification of marine current energy converters in constrained flow fields," Ph.D. dissertation, University of Southampton, Southampton, United Kingdom, 2016.
[9] T. Nishino and R. H. J. Willden, "The efficiency of an array of tidal turbines partially blocking a wide channel," *Journal of Fluid Mechanics*, vol. 708, pp. 596–606, 2012.
[10] J. McNaughton, B. Cao, C. R. Vogel, and R. H. J. Willden, "Model scale testing of multi-rotor arrays designed to exploit constructive interference effects," in *Proceedings of the 13th European Wave and Tidal Energy Conference*, Naples, 2019.
[11] J. Schluntz and R. H. J. Willden, "The effect of blockage on tidal turbine rotor design and performance," *Renewable Energy*, vol. 81, pp. 432–441, 2015.
[12] C. R. Vogel and R. H. J. Willden, "Multi-rotor tidal stream turbine fence performance and operation," *International Journal of Marine Energy*, vol. 19, pp. 198–206, 2017.
[13] "Unsteady loading tidal turbine benchmarking study," https://supergen-ore.net/projects/tidal-turbine-benchmarking, (accessed Jan. 25, 2023).
[14] S. W. Tucker Harvey, X. Chen, D. Rowe, J. McNaughton, C. R. Vogel, K. Bhavsar, T. Allsop, J. Gilbert, H. Mullings, T. Stallard, A. Young, I. Benson, and R. H. J. Willden, "Design and testing of a benchmarking tidal turbine," in *Proceedings of the European Wave and Tidal Energy Conference*. EWTEC, 2023, p. 574.
[15] D. D. Apsley, T. Stallard, and P. K. Stansby, "Actuator-line CFD modelling of tidal-stream turbines in arrays," *Journal of Ocean Engineering and Marine Energy*, vol. 4, no. 4, pp. 259–271, 2018.
[16] A. Wimshurst and R. H. J. Willden, "Spanwise flow corrections for tidal turbines," *International Marine Energy Journal*, vol. 1, no. 2 (Nov), pp. 111–121, 2018.
[17] W. Z. Shen, R. Mikkelsen, J. N. Sørensen, and C. Bak, "Tip loss corrections for wind turbine computations," *Wind Energy*, vol. 8, no. 4, pp. 457–475, 2005.
[18] S. Ettema, "Novel Turbine Fence Optimisation Using Lateral Flow Constraint," Ph.D. dissertation, University of Oxford, Oxford, United Kingdom, 2022.
[19] C. R. Vogel, G. T. Houlsby, and R. H. J. Willden, "Effect of free surface deformation on the extractable power of a finite width turbine array," *Renewable Energy*, vol. 88, pp. 317–324, 2016.
[20] N. Kolekar, A. Vinod, and A. Banerjee, "On blockage effects for a tidal turbine in free surface proximity," *Energies*, vol. 12, no. 17, 2019.